On the Correlation between Mechanical Flexibility, Nanoscale Structure, and Charge Storage in Periodic Mesoporous CeO_2 Thin Films

Torsten Brezesinski,[†,§,*] John Wang,[‡,∥] Robert Senter,[†] Kirstin Brezesinski,[§] Bruce Dunn,[‡,⊥,*] and Sarah H. Tolbert[†,⊥,*]

[†]Department of Chemistry and Biochemistry, University of California at Los Angeles, Los Angeles, California 90095-1569, [‡]Department of Materials Science and Engineering, University of California at Los Angeles, Los Angeles, California 90095-1595, [§]Institute of Physical Chemistry, Justus-Liebig-University Giessen, Heinrich-Buff-Ring 58, 35392 Giessen, Germany, and [⊥]California NanoSystems Institute, University of California at Los Angeles, Los Angeles, California 90095. [∥]Current address: HRL Laboratories, LLC, Malibu, California 90265.

ABSTRACT In this work, we report the synthesis and characterization of highly ordered mesoporous CeO_2 thin films with crystalline walls. While this article focuses on electrochemical studies of CeO_2 with periodic nanoscale porosity, we also examine the mechanical properties of these films and show how pore flexing can be used to facilitate intercalation of lithium ions. Mesoporous samples were prepared by dip-coating using the large diblock copolymer KLE as the organic template. We establish that the films have a mesoporous network with a biaxially distorted cubic pore structure and are highly crystalline at the atomic scale when heated to temperatures above 500 °C. Following a previously reported approach, we were able to use the voltammetric sweep rate dependence to determine quantitatively the capacitive contribution to electrochemical charge storage. The net result is that mesoporous CeO_2 films exhibit reasonable levels of pseudocapacitive charge storage and much higher capacities than samples prepared without any polymer template. Part of this increased capacity stems from the fact that these films are able to expand normal to the substrate upon intercalation of lithium ions by flexing of the nanoscale pores. This flexing relieves stress from volume expansion that normally inhibits charge storage. Overall, the results described in this work provide fundamental insight into how nanoscale structure and mechanical flexibility can be used to increase charge storage capacity in metal oxides.

KEYWORDS: mesoporous materials · ceria · CeO_2 · electrochemical charge storage · supercapacitors · pore flexibility · block copolymer templating · nanostructured materials

In recent years, it has been shown that thin films with well-ordered nanoscale porosity can be readily formed by co-assembly of inorganic oligomers with organic templates using evaporation-induced self-assembly (EISA).[1−3] Despite the fact that a broad range of ordered porous materials can be made, the majority of the polymer-templated materials do not allow the inorganic walls to be crystallized while retaining nanoscale order. For example, it has been shown that, when mesostructured thin films with 10−15 nm repeat distances and 3−6 nm thick walls are produced, the nanoscale structure is not well preserved after crystallization, and in most cases, the porosity is ill-defined.[4,5] In this work, we show that mesoporous materials can be produced that possess both fully crystalline walls and well-ordered porosity by utilizing a templated structure with larger repeat distance and thicker pore walls. Here, we utilize a large poly(ethylene-*co*-butylene)-*b*-poly(ethylene oxide) diblock copolymer (also referred to as KLE), which allows the formation of cubic architectures with 20−30 nm pore-to-pore distances and 10−15 nm thick walls.[6−9] These thicker walls allow for the formation of stable crystallites without the need to distort the pore network to accommodate crystallization and grain growth. This work focuses on ceria (CeO_2), a material that we show how to synthesize with highly periodic nanoscale porosity and fully crystalline walls. We use this mesoporous CeO_2 as a model system for studying charge storage in nanoscale metal oxides.

Ceria is of potential interest for a wide range of applications including catalysis, oxygen gas sensing, and as the electrolyte in solid oxide fuel cells.[10−12] Ceria is also a feasible material for charge storage because of the ability of cerium to cycle between different redox states.[13,14] Unlike many traditional battery materials, however, CeO_2 does not have a layered or tunnel structure.[15,16] As a result, electrochemical redox reaction rates in the bulk material are quite slow, which limits its usefulness for electrochemical charge storage devices.

*Address correspondence to tolbert@chem.ucla.edu, bdunn@ucla.edu, torsten.brezesinski@phys.chemie.uni-giessen.de.

Received for review July 3, 2009 and accepted December 17, 2009.

Published online January 26, 2010. 10.1021/nn9007324

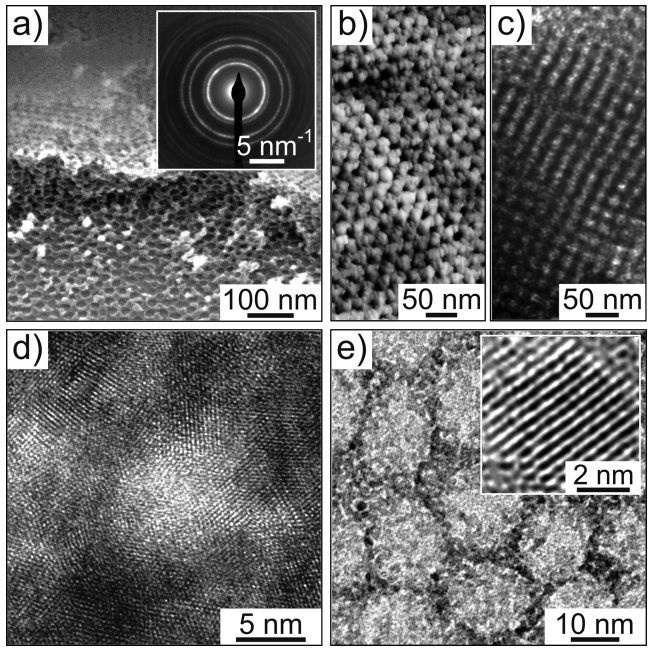

Figure 1. Nanoscale structure of "thick" (a−d) and "thin" (e) cubic mesoporous CeO_2 films that had been calcined at 600 °C in air. (a) Cross-sectional FESEM image. An electron diffraction pattern showing sharp Debye−Scherrer rings characteristic of cubic cerianite is given in the inset. (b) Tapping-mode AFM image of the hexagonal top surface. (c) Low-magnification bright-field TEM image. (d) HRTEM image from the same sample shown in (b,c). (e) High-magnification bright-field TEM image of a 9 nm thick CeO_2 film with honeycomb structure. A HRTEM image of a single cerianite grain is shown in the inset.

Creating nanostructured versions of this material could be a viable solution to this problem because of the ability to access both bulk and surface redox sites.[17] Electrochemical properties can potentially benefit from short diffusion path lengths for ion transport and the increased opportunity for surface faradaic reactions.[18,19] Ceria thus serves as a model system to examine how nanoscale porosity can be used to increase charge storage rates in materials that show very sluggish kinetics in bulk form. Because of the exquisite nanometer-scale periodicity of the materials discussed here, we are further able to use small-angle X-ray scattering to analyze how the mechanical properties of the porous framework complement the high surface area and short diffusion path lengths in facilitating charge storage.

Three different charge storage mechanisms are feasible when a material is immersed in an electrolyte: (1) cations can be stored in a thin double layer at the electrode/electrolyte interface (nonfaradaic mechanism); (2) cations can interact with the bulk of an electroactive material which then undergoes a redox reaction or phase change, as in conventional batteries (faradaic mechanism); or (3) cations can electrochemically adsorb onto the surface of a material through charge transfer processes (faradaic mechanism). The latter mechanism is a pseudocapacitive effect (often referred to as redox pseudocapacitance) because the cations are faradaically stored but do not react with the bulk of the material or require a phase change.[20,21] Currently, there is widespread interest in using pseudo-capacitor-based materials for electrochemical capacitors because the energy density associated with faradaic reactions is substantially larger, by at least 1 order of magnitude compared to electric double-layer capacitors. At the same time, power densities can be much higher compared to conventional batteries because phase transitions and long-range solid-state diffusion of ions are not required for charge storage.

In this work, we describe the preparation of mesoporous sol−gel-type CeO_2 thin films and characterize their electrochemical properties using solution-based voltammetry experiments. Through these experiments, the relationships among surface area, charge storage capacity, and charge/discharge rates are examined and compared to nontemplated samples. Electrochemical impedance spectroscopy measurements are used to gain additional insight regarding double-layer and pseudocapacitive contributions. Lastly, X-ray scattering measurements are used to examine the mechanical changes that result from the intercalation of lithium ions into the cerianite lattice. By correlating mechanical changes with redox activity, we are able to identify some of the unique advantages of using porous architectures for electrochemical materials. As mentioned above, bulk ceria does not show facile charge storage characteristics, and precisely because of this, it is an excellent test bed for determining how nanoscale porosity can be used to enhance charge storage efficiency in nanostructured metal oxides.

RESULTS AND DISCUSSION

Nanoscale Structure. Mesoporous ceria films were synthesized using a procedure adapted from that of Smarsly *et al.*[22] Briefly, an ethanolic solution containing the ceria precursor and structure-directing agent is dip-coated onto a polar substrate. On evaporation of the solvent, the system co-assembles to form a mesostructured inorganic/organic composite. With thermal treatment, this composite develops a unique pore-solid architecture with fully crystalline walls as described below.

Figure 1a presents a field emission scanning electron microscope (FESEM) image taken at a 45° tilt of a cut in a KLE-templated CeO_2 film. This micrograph shows a cubic architecture with 14 nm diameter pores and emphasizes the homogeneity of the three-dimensional interconnected structure. Moreover, it can be observed that the films are crack-free, which suggests that nanoscale ceria effectively withstands the stress that develops over the course of thermal treatment, especially that arising from crystallization of the initially amorphous pore walls. The homogeneity of the self-organized samples employed in this work is also evident from atomic force microscopy (AFM, Figure 1b) and transmission electron microscopy (TEM, Figure 1c).

The tapping-mode AFM image in Figure 1b further shows that the pores at the air−solid interface are open and that the top surface is fairly flat; the root-mean-square (rms) roughness is less than 2 nm. From high-resolution TEM (HRTEM, Figure 1d) and electron diffraction (Figure 1a, inset), we are able to establish that the sub-15 nm thick pore walls are highly crystalline with randomly oriented cerianite grains. Physisorption data obtained on samples that had been thermally treated at 550 °C provide a Brunauer−Emmett−Teller (BET) surface area of approximately 150 $m^2\ g^{-1}$ and a porosity of 30−35%.[22]

Figure 1e presents a high-magnification TEM image of an ultrathin KLE-templated film with 16−18 nm diameter pores arranged on a two-dimensional lattice. The film thickness is only 9 nm. Interestingly, the pores of such a monolayer sample are somewhat larger compared to 13−14 nm diameter pores observed with thicker films (>100 nm) produced under otherwise identical conditions. Figure 1e further shows a high-resolution TEM image of a single cerianite nanocrystal of the same film, which underscores the high degree of crystallinity.

These microscopy results are further supported by two-dimensional small-angle X-ray scattering (2D-SAXS) data. The patterns shown in Figure 2 were collected at two different angles of incidence, β (defined as the angle between the X-ray beam and the plane of the substrate), on Beamline 1-4 at the Stanford Synchrotron Radiation Laboratory. For $\beta < 15°$, the self-organized films (Figure 2a,b) produce distinct scattering maxima that can be indexed to a face-centered cubic (fcc) pore structure with (111) orientation relative to the plane of the substrate. Despite significant unidirectional lattice contraction (>60% normal to the substrate) upon calcination, both in-plane and off-specular scattering maxima are still well-defined after treatment of films at 800 °C. Second-order reflections can also be observed, indicating both the high degree of pore ordering and the remarkable thermal stability of the cubic architecture. 2D-SAXS patterns obtained at $\beta = 90°$ (Figure 2c, transmission mode) show strong maxima with no indications of in-plane lattice contraction. The presence of spots instead of rings suggests that these films contain very large domains in the plane of the substrate.[9,23] The full width at half-maximum (fwhm) intensity of these scattering maxima is less than 20°, despite the fact that the 30 μm silicon substrates used were coated on both sides for experimental reasons, and so the X-ray beam was actually going through two separate films (one on each side of the substrate) with uncorrelated domain orientations. Taking into account the data obtained from electron microscopy, we postulate that the individual domains have a size of more than 100 μm. The reason for the formation of such large mesostructured domains is not fully understood at this point.

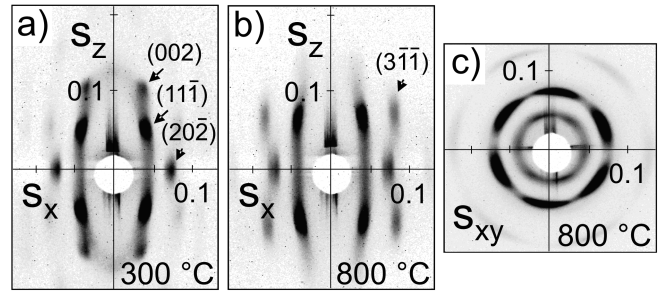

Figure 2. Temperature-dependent 2D-SAXS data for KLE-templated CeO_2 films. The patterns were taken at angles of incidence β of 8° (a,b) and 90° (c) and show the evolution of the biaxially distorted fcc mesopore structure as a function of annealing temperature. Scattering vector *s* components are given in units of 1/nm with $s = 2/\lambda \sin\theta$ (λ is the wavelength and θ the scattering angle).

To track the nanocrystal growth in the pore walls, synchrotron-based wide-angle X-ray scattering (WAXS) measurements were conducted on the KLE-templated samples. Figure 3 shows typical temperature-dependent WAXS data from a 300 nm thick film. The crystallization begins at around 300 °C, leading to rather small crystallites with an average size of 2 nm. Identification of the main peaks and relative intensities is found to match the cubic cerianite phase according to JCPDS reference card #34-0394 (CeO_2 has only one polymorph, namely, the cubic fluorite-type structure). The fact that the peak intensity increases slowly and the fwhm intensity decreases with higher annealing temperatures suggests gradual nanocrystal growth in the pore walls. Scherrer analysis of the grain size indicates a crystallite diameter of 12−13 nm at 800 °C. This size corresponds well with the pore wall thickness obtained from electron microscopy. Annealing temperatures of more than 800 °C, however, lead to a rapid increase in crystallite size accompanied by restructuring and loss of nanoscale periodicity. We note that the initial domain size of just 2 nm is quite small. If this value is assumed to be the stable critical nucleation size, it helps explain the excellent retention of nanometer-scale periodicity observed for high-temperature calcination in Figures 1 and 2. Stable nuclei which are much smaller than the pore walls should allow for uniform nucleation and growth of the crystalline phase with retention of the periodicity. If larger nuclei are present at the onset of crystallization, more restructuring of the pore system is likely to occur. Consistent with this hypothesis is the

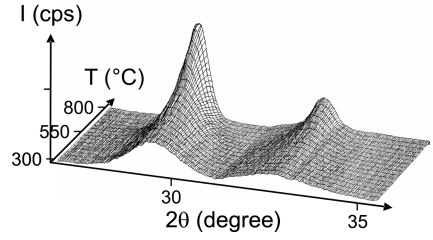

Figure 3. *In situ* temperature-dependent WAXS data for cubic mesoporous CeO_2. The pattern shows the evolution of the (111) and (200) peaks of cerianite with annealing temperature.

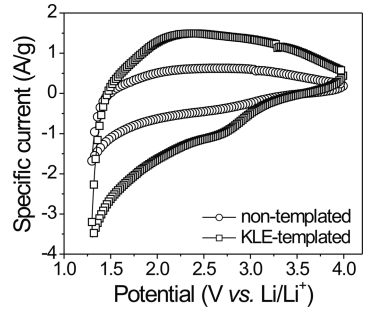

Figure 4. Gravimetrically normalized cyclic voltammetric responses for KLE-templated and nontemplated CeO_2 films at a sweep rate of 20 mV/s.

fact that crystalline ceria/surfactant composites with well-ordered nanoscale periodicity and wall thicknesses of only a few nanometers have been reported in the literature.[24]

Electrochemical Properties. To examine the redox processes present in sol−gel-type CeO_2 thin films, solution-based voltammetry experiments were performed. All measurements described in the ensuing section were conducted on samples that had been thermally treated at 600 °C in air. Figure 4 shows typical cyclic voltammograms (CVs) for both 90 nm thick KLE-templated films and for 95 nm thick samples produced without any polymer template. We will refer to these template-free samples as nonporous because they lack large-scale mesoporosity. As they were produced *via* sol−gel methods, however, they likely contain some microporosity. The shape of the CV curves is similar to previously reported data for e-beam deposited films (cathodic and anodic peaks at 1.3 and 2.0 V *vs* Li/Li^+, respectively).[25,26] The KLE-templated samples, however, show an additional cathodic shoulder peak at around 2.8 V.

The area under the CV curves represents the total amount of stored charge, which arises from both faradaic and nonfaradaic processes. Figure 4 clearly indicates that the charge storage is strongly dependent upon film morphology. At a sweep rate of 20 mV/s, the volume normalized charge storage is calculated to be 65 $mC/cm^2/\mu m$ for mesoporous CeO_2 samples and only 41 $mC/cm^2/\mu m$ for nontemplated ones. By comparison, previously reported e-beam deposited films, which likely have very little internal porosity, displayed an even lower value at the same sweep rate (Table 1).[25] Since these values are volume normalized, however, and the density of the mesoporous ceria should be significantly less than either the nontemplated sol−gel samples or e-beam derived dense films, these values underestimate the improvements produced by nanoscale porosity on a mass normalized basis.

TABLE 1. Amount of Charge Stored in the Various CeO_2 Thin Film Materials at a Sweep Rate of 20 mV/s

sample	stored charge ($mC/cm^2/\mu m$)	x in Li_xCeO_2
KLE-templated	65	0.24
nontemplated	41	0.10
e-beam deposited	19	0.046

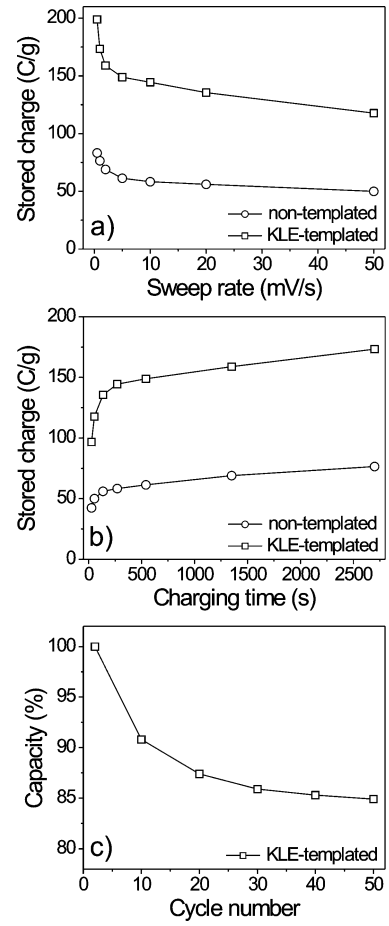

Figure 5. Charge storage dependence on sweep rate (a) and comparison of charging rates (b) for KLE-templated and nontemplated CeO_2 films. (c) Charge storage capacity as a function of cycle number for mesoporous CeO_2 at a sweep rate of 5 mV/s.

As shown in Figure 5a, the total charge storage is also observed to be strongly dependent upon sweep rate. With decreasing sweep rate, the amount of charge stored increases, which implies that full storage has not been achieved because of kinetic limitations associated with the diffusion of Li^+ through the bulk of the films. Regardless of the sweep rate, however, the magnitude of total charge storage (gravimetrically normalized) for mesoporous CeO_2 is approximately 2.5 times larger than that of the bulk films. For example, as shown in Figure 5b, at a sweep rate of 0.5 mV/s (charging time of 5400 s), the mole fraction of stored lithium is calculated to be 0.35 (198 C/g) and 0.14 (83 C/g) for mesoporous and nonporous materials, respectively. By comparison, after only 54 s of charging (sweep rate of 50 mV/s), the mesoporous and nonporous films have stored 120 and 50 C/g, respectively. KLE-templated CeO_2 samples also show very good cycling characteristics with a capacity fade of only 14−15% after 50 cycles (Figure 5c).

Taken together, the results demonstrate that the introduction of 3-dimensional interconnected porosity significantly enhances electrochemical charge storage properties and leads to faster charge/discharge kinetics. The combination of electrolyte access through the mesoporous network and short diffusion path lengths for both electronic and ion transport provides a beneficial microstructure for Li^+ insertion/extraction and the accompanying redox reactions.[17]

The total charge stored can be separated into three components: the faradaic contribution from Li^+ intercalation, the faradaic contribution from charge transfer processes with atoms located at the surface, referred to as pseudocapacitance, and the nonfaradaic contribution from the double-layer effect. The kinetic limitations associated with traditional Li^+ insertion are quite different from those associated with surface redox processes. Insertion is a diffusion-controlled process and, thus, the current flow at any given voltage is expected to vary with the square root of the sweep rate.[27] By contrast, surface redox processes are not diffusion-controlled and, thus, the current should vary linearly with the sweep rate.[28] By measuring current as a function of sweep rate for a variety of voltages, it is possible to separate the Li^+ insertion and capacitive contributions to electrochemical charge storage.[28,29] This method was applied recently to the study of mesoporous TiO_2 films, and the results indicated that for samples made from preformed nanocrystalline building blocks, about half of the total stored charge is capacitive in nature.[19,21]

The capacitive contributions to charge storage for KLE-templated and nontemplated CeO_2 films are shown in Figure 6. These data were collected after several cycles, once the charge storage capacity had reached consistent values. In Figure 6a, the voltage profile for the capacitive current (shaded area) determined from analyzing Figure 4 is compared to the total current from the experimentally obtained current−voltage response. The calculation indicates that the capacitive contribution varies with the sweep rate (or charging time) for the mesoporous films. At the faster sweep rate of 10 mV/s (charging time of 270 s), nearly all of the current arises from capacitive processes. At the slower sweep rate of 0.5 mV/s (charging time of 5400 s), the capacitive contribution accounts for some 70% of the total current. The reason for this decrease is that the longer charging time enables more current to be contributed from diffusion-controlled intercalation processes (Figure 6b). The mesoporous films have effectively achieved their maximum capacitive contribution of about 135 C/g after a charging time of ~130 s. Longer charging times lead to a greater contribution from intercalation processes. Thus, in Figure 6b, the results at 0.5 mV/s have a similar amount of capacitive charge storage to that of the 10 mV/s sweep rate but a much larger intercalation component. The voltammetric response for the nonporous CeO_2 films exhibits similar behavior with primarily a capacitive response at shorter time and increasing charge storage from intercalation at longer times. However, the magnitude of the total charge storage from both capacitance and intercalation for the mesoporous films is much larger than that of the nonporous samples.

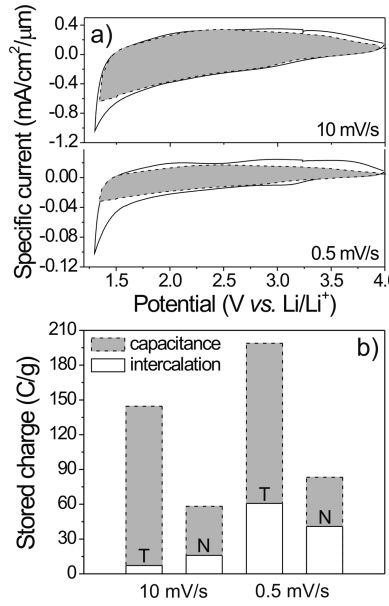

Figure 6. (a) Voltammetric responses for KLE-templated CeO_2 films at sweep rates of 10 and 0.5 mV/s. The voltage profile for the capacitive current is shown as the shaded region. (b) Comparison of the total stored charge for templated (indicated by T) and nontemplated (indicated by N) samples. The stored charge is divided into Li^+ intercalation and capacitive contributions.

The results clearly show that both capacitance and intercalation storage processes benefit from the mesoporous morphology, which enables electrolyte access to the electrochemical sites and provides short diffusion path lengths.[17] In this way, materials which do not normally show high charge storage capacity or facile charging kinetics, but which might be attractive for other reasons such as cost or environmental properties, can be improved.

Figure 7 presents galvanostatic discharge curves at a rate of *C*/2 for both mesoporous and nonporous CeO_2. Again, these data were collected after several cycles, after the charge storage capacity had reached consistent

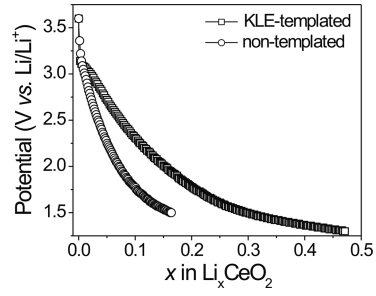

Figure 7. Galvanostatic discharge curves for KLE-templated and nontemplated CeO_2 films at a rate of *C*/2.

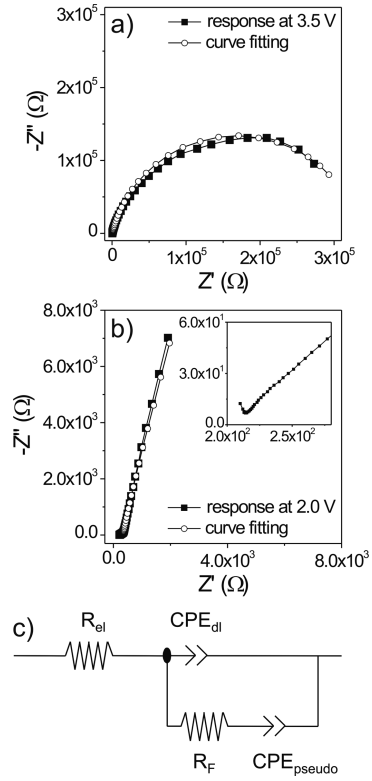

Figure 8. (a,b) Nyquist representations of impedance data for KLE-templated CeO_2. The responses at 3.5 and 2.0 V *vs* Li/Li^+ as well as model fit data are shown. An expansion of the low Z' region of (b) is shown in the inset. (c) Circuit model describing the impedance behavior of CeO_2 thin film electrodes in nonaqueous electrolytes.

values. These curves show the profound effect that mesoporosity has on Li^+ intercalation as significantly more lithium can be stored in the porous material compared to the denser counterpart. Although not shown here, a small, relatively flat region at around 3.1 V *vs* Li/Li^+ is observed for the mesoporous films. This region corresponds well with the shoulder peak in Figure 4, although at a sweep rate of 20 mV/s, this peak is shifted toward lower potentials, presumably because of the finite electronic resistance of CeO_2. A closer examination of Figure 7 also shows that the discharge curves behave almost linearly in the range between 2 and 3 V for both templated and nontemplated films. This behavior is expected as it represents a typical capacitive discharge.[30] The shallower slope observed for mesoporous samples is consistent with this material having higher capacitance. For example, if the potential is kept at 2 V *vs* Li/Li^+, the nontemplated films are capable of storing 0.07 mol of lithium, while for mesoporous samples, the mole fraction is greater than 0.15.

Electrochemical impedance spectroscopy (EIS) measurements were also carried out to gain additional insight into the interfacial behavior of the mesoporous films. By using appropriate models, it is possible to distinguish pseudocapacitance from double-layer capacitance by analyzing the impedance over a range of frequencies between 0.1 Hz and 100 kHz. Figure 8a,b shows impedance spectra for mesoporous CeO_2 samples at 3.5 and 2.0 V *vs* Li/Li^+. In the circuit model, one can use either simple capacitors for both the double-layer and pseudocapacitance, or one can employ a constant phase element (Z_{CPE}) which allows for a distribution of capacitance values. For surface charge storage in a material with disordered surface structure like those used here, the constant phase element often produces better fits to the data. Z_{CPE} is given by the following equation:

$$Z_{CPE} = [B(j\omega)^n]^{-1} \quad (1)$$

with B and n ($0 < n < 1$) as frequency-independent proportionality constants.[31] In the limit of $n = 1$, ideal capacitor behavior is observed.[32] According to Conway, the circuit model shown in Figure 8c can be used to describe the electrochemical impedance behavior of CeO_2 thin film electrodes in nonaqueous electrolytes.[33] R_{el} and R_F represent the resistance of the electrolyte solution and the faradaic charge transfer resistance, respectively. Since pseudocapacitance arises from a potential-dependent interfacial redox reaction, a faradaic charge transfer resistance in series with a pseudocapacitance, CPE_{pseudo}, suggests that electron charge transfer is involved in the charging/discharging process. In addition, the nonfaradaic current for double-layer charging, CPE_{dl}, is in parallel with the faradaic charge transfer resistance.

The specific capacitance for KLE-templated CeO_2 at three different applied potentials was derived from numerical fitting to the circuit model in Figure 8c. The results are shown in Figure 9. For potentials above 3 V, only a very small double-layer capacitance is observed due to the high electronic resistance of ceria, consistent with having all Ce in the fully oxidized state. At lower potentials, Li^+ intercalation occurs and a sizable fraction of Ce reduces to Ce^{3+}. Electronic conductivity increases from electron hopping processes, and the films reveal significant amounts of capacitance; pseudocapacitive contributions increase with decreasing voltage, while double-layer contributions are mostly voltage-independent. The value of n for CPE_{pseudo} is greater than 0.9, indicating nearly ideal capacitor behavior. Thus, when a simple capacitor is substituted for Z_{CPE} in the circuit shown in Figure 8c, the results are qualitatively

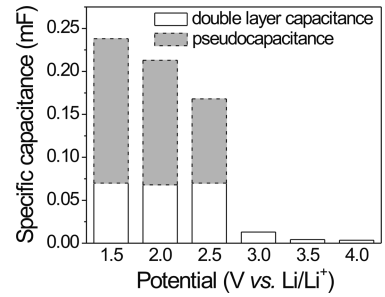

Figure 9. Dependence of the specific capacitance upon applied potential for KLE-templated CeO_2 films.

similar with capacitance values changing by only ~10%. The conclusion from this measurement is thus a corroboration of the dominant role played by pseudocapacitance in these materials—by building nanoscale porosity into redox active materials, respectable levels of charge storage can be created through pseudocapacitive mechanisms even though the materials exhibit slow kinetics in bulk form.

Mechanical Properties. The slow lithium ion intercalation kinetics of bulk ceria arises from the fact that the CeO_2 crystal structure contains neither van der Waals gaps nor one-dimensional tunnels where lithium ions can easily diffuse and be stored. To accommodate Li^+ intercalation, expansion of the ceria lattice is needed, and this structural change is a kinetically slow process. Moreover, in bulk materials, the strain associated with partial Li^+ incorporation inhibits further intercalation. Mesoporous networks, however, can be modeled as a nanotruss architecture.[34,35] The ability to flex the framework of a metal oxide can be quite favorable for Li^+ incorporation as changes in the nanoscale structure can be used to accommodate the strain associated with intercalation processes. Ceria is an ideal system for studying these effects for two reasons. In the first place, the large lattice strains that occur upon intercalation should produce significant changes in nanoscale structure that can be easily measured. Second, the highly periodic nature of the mesoporous ceria used here facilitates structural characterization of the pore architecture.

To examine the expansion that results from the intercalation of lithium ions into the ceria lattice, one-dimensional small-angle X-ray scattering (1D-SAXS) measurements were carried out. While changes in pore structure are usually rather difficult to measure, the ordered pore-solid architecture provides an opportunity to follow small changes in the periodic system.[36] Figure 10a shows diffraction from the nanoscale periodicity of the porous ceria before and after Li^+ intercalation. The fully lithiated film reveals a significant shift in the peak position to lower angle or larger repeat distance. This expansion of the nanoscale periodicity is used to accommodate the atomic-scale expansion of individual ceria grains upon intercalation of Li^+. The overall result is an expansion of about 10% in the periodicity of the film normal to the substrate. Interestingly, this expansion does not result in the loss of order as the peak intensity is only slightly decreased. These data provide key evidence in our quest for understanding why nanoscale porosity is so beneficial in facilitating both intercalation and capactive charge storage.

While the shift in peak position shown in Figure 10a is the most dramatic result, fits to the data also indicate that, contrary to expectations for a strained system, the peak position does not broaden upon Li^+ intercalation. Instead, there is a decrease in the fwhm intensity of the (111) peak by 0.08°. This indicates that

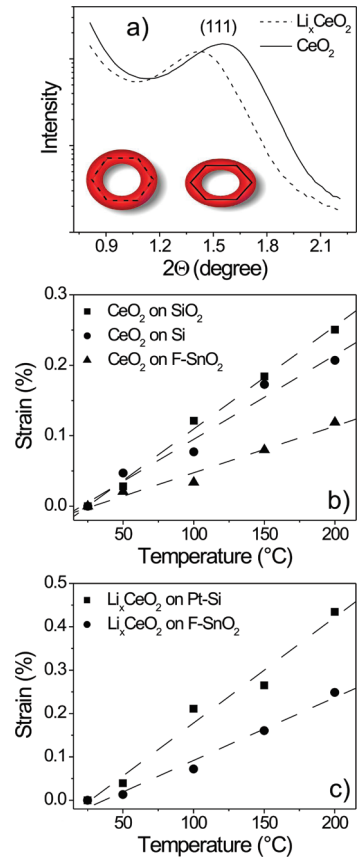

Figure 10. (a) Typical 1D-SAXS pattern for KLE-templated CeO_2 and Li_xCeO_2 films. (b,c) Experimentally determined strains of cubic mesoporous CeO_2 and Li_xCeO_2 films on different substrates as a function of temperature as well as fit data (dashed lines). To fully charge the films, the potential was kept at 1.5 V *vs* Li/Li^+ for 2 h.

intercalation may actually relieve in-plane stress. To understand this result, some discussion of the strains associated with film formation is needed.

For all of the mesoporous materials that we have examined, the fwhm intensity of the out-of-plane diffraction peaks always increased upon calcination and removal of the structure-directing agent.[36] In the synthesis of these templated sol−gel materials, after deposition from solution, an inorganic/organic composite is formed that is bound to the substrate but has a low density, hydrated inorganic wall structure. Thermal treatment both removes the organic template and condenses the inorganic framework. This condensation results in a decrease in inorganic volume. Since the film is bound to the substrate, this stress can only be accommodated by a decrease in pore spacing normal to the substrate. Our data indicate that the stress gradient is not uniform throughout the film, however. Pores at the film/substrate interface are the most stressed, and this relaxes through the thickness of the film. This stress gradient produces a gradient in pore deformation that correlates with the increase in the diffraction peak fwhm intensity.

A typical calcined sol−gel-type film thus has tensile (expansive) stress imposed by the substrate. Intercalation of lithium ions into the film should lead to an expansion of the lattice, resulting in a compressive stress set up by the substrate. As long as the stress resulting from intercalation is less than the stress generated in forming the film, however, the overall stress state should be lower in the lithiated sample. The concept expressed here is straightforward: the use of a prestrained system to improve insertion kinetics in materials where volume expansion upon Li^+ insertion is limiting has exciting potential for the design of new materials for energy storage.

While changes in small-angle diffraction upon lithiation show the most direct effects of stress in these nanoporous materials, related SAXS experiments provide us with a means to further quantify these mechanical changes. A specific question is—what is the correlation between the out-of-plane deformations shown in Figure 10a and changes in the in-plane stress? To probe this relationship, we examined the Poisson's ratio, which relates the resulting transverse strain with applied strain. Since strain and stress are related through the Young's modulus, the Poisson's ratio can also be viewed as providing information about the films' ability to relieve in-plane stress by out-of-plane deformations.

To accomplish this, we use a modification of the widely employed Stoney's equation for examining macrostress in thin films on thick substrates.[36,37] In the original form, the effect of stress from a coating is associated with deformation or bending of the substrate. In our case, we directly examine the deformation in the coating using small-angle X-ray scattering from the nanoscale porosity. For a given film, the out-of-plane pore displacement is related to the mismatch in the thermal expansion between a film and the substrate. By heating a thin film sample under controlled conditions, the substrate can thus be used to put the sample under either tensile or compressive strain, depending on the relative thermal expansion coefficient of the film and the substrate. By measuring the change in pore spacing normal to the strain direction, information about Poisson's ratio can be obtained (eq 2). Equation 2 has two unknowns, the thermal expansion coefficient (α_f) and Poisson's ratio (ν). To solve for both of these unknowns, the change in out-of-plane strain (ε_3) as a function of temperature (T) is probed on multiple substrates with different thermal expansion coefficients (α_s) using SAXS.

$$\varepsilon_3 = \left(\frac{1+\nu}{1-\nu}\alpha_f - \frac{2\nu}{1-\nu}\alpha_s\right)\Delta T \qquad (2)$$

For the non-intercalated CeO_2 films, three substrates were used, namely, fused silica,[38] fluorine-doped SnO_2 (FTO),[38] and (100)-oriented silicon wafer.[39] As the FTO is a fairly thin layer on a glass substrate, it is the thermal expansion coefficient of glass that determines the thermally generated strain. To probe the lithiated films, Li_xCeO_2, a conducting substrate was needed to electrochemically insert Li^+ into the CeO_2. Therefore, platinized silicon and FTO were used. The samples were first heated to 300 °C under flowing nitrogen to drive off water, cooled, and then diffraction patterns were obtained at different temperatures. The shift of the fundamental small-angle diffraction peak is small but detectable, and in order to obtain the best results, the instrument was set to the highest resolution and a mirror−mirror ($\theta-2\theta$) geometry was utilized. The patterns were then peak fitted to remove the influence of the baseline. From these data, a plot of strain *versus* temperature for each substrate can be produced (Figure 10b,c). On a substrate with low thermal expansion, we see a large mismatch in the expansion of the substrate and the films, leading to significant out-of-plane peak shifts. As substrates with larger coefficients of thermal expansion are used, the difference is minimized and smaller peak shifts are observed.

By fitting the slopes on different substrates, strain as a function of temperature can be obtained and, eq 2 can be solved for the two unknowns—thermal expansion coefficient and Poisson's ratio of the film. For the mesoporous CeO_2 samples, a thermal expansion coefficient of 7.8×10^{-6} °C^{-1} is obtained. This value is less than the literature values for bulk ceria of 11.58×10^{-6} °C^{-1} obtained using dilatometry over the temperature range from 298 to 1123 K.[40] While part of this difference might be due to the nanoscale porosity, measurements over the temperature range from 298 to 1473 K produced a higher value of 12.68×10^{-6} °C^{-1}.[40] Our numbers were measured in the range from 323 to 473 K, and so a smaller value is expected. Utilizing this same technique, we found the thermal expansion coefficients of porous silica films with similar ordered porosity match the plethora of literature values for sol−gel-type silica.[41]

If now we examine the Poisson's ratio, we obtain a value of 0.38 ± 0.02, which is elevated from the literature value of 0.294 and higher than the range of 0.1−0.3 typically allowed for isotropic materials.[42,43] This large value is not unexpected, however, as we have obtained Poisson's ratios this large and larger on other ordered porous oxides such as SiO_2, TiO_2, *etc*.[36] While these materials nominally have a cubic pore system, the shrinkage normal to the substrate upon calcination breaks the cubic symmetry and makes Poisson's ratios greater than 0.3 allowable. A more intuitive way to consider this increase is to model the pores as hexagons with hinged joints (Figure 10a, inset). Geometrically, if the hexagon is compressed in the plane of the film, as in the cartoon on the right, in-plane strain will have a greater effect on out-of-plane displacements compared to ideal hexagons, and so the Poisson's ratio will be greater.

As discussed above, the pores expand in the free direction upon intercalation of lithium ions. If the analysis described above is repeated on a fully lithiated CeO_2 film, we see a large increase in thermal expansion coefficient to 13.4×10^{-6} C^{-1}. Also, the samples reveal a smaller Poisson's ratio of 0.33 ± 0.02. This value is now much closer to the maximum theoretical value of 0.3 expected for a cubic system. Using the jointed hexagon model described above, lithium intercalation reverses the compressive effects of calcination and moves the porosity back toward the ideal structure produced in the original self-organization process. This is depicted graphically in the cartoon on the left in Figure 10a, inset. Thus, the fact that the expanded pore yields a lower Poisson's ratio further supports the hypothesis that not only do the pores flex to minimize in-plane strain but their shape influences their ability to do so.

Together, these results indicate a potentially new way to minimize the expansive strains associated with lithium ion intercalation by introducing compensating strains in the material during synthesis. While complex epitaxial matching is usually required to engineer strain into materials using bond length mismatch, the present work shows that flexible pores provide a facile method to introduce similar strains into materials through flexing of a nanotruss architecture. Moreover, because of the highly regular geometry of these templated nanoscale pores, the compressive strains that are introduced are homogeneous and easily reversed upon Li^+ intercalation. It is an interesting question for future studies to consider whether porous ceria with a disordered pore system (for example, conventional sol−gel derived ceria with a fractal pore structure[44]) would show similar correlations between mechanical properties and electrochemical charging. Fractal pore systems tend to flex more easily than the fully interconnected pores employed here, and so we speculate that while conventional sol−gel derived ceria might be able to accommodate the volume expansion associated with Li^+ insertion, it would not be prestrained to facilitate this insertion.

CONCLUSIONS

In this work, we described the synthesis and characterization of polymer-templated mesoporous ceria. Because of the nature of the block copolymer template employed, materials with both fully crystallized walls and a high degree of nanoscale pore periodicity could be produced. While ceria is a redox-active material, bulk CeO_2 is not an interesting material for charge storage as it displays low capacity and slow kinetics. In mesoporous form, however, both insertion capacity and pseudocapacitance increase significantly. The result is that mesoporous ceria exhibits reasonable electrochemical energy storage properties.

The polymer-templated mesoporous ceria described here does not, however, set new records for energy or power density. Instead, the value of this work is in understanding how nanoscale porosity can be used to convert a nonactive metal oxide into an active one. The increase in pseudocapacitance is easy to understand and is a direct result of the increased surface area in mesoporous ceria compared to the nontemplated material. Redox chemistry at surface cerium sites is facile as Li^+ intercalation into the lattice is not required, and therefore, slow solid-state ion diffusion and strain induced by volume expansion do not limit this process. As our previous work with mesoporous titania illustrates,[19] the total pseudocapacitance could likely be increased even further if preformed nanocrystalline building blocks rather than molecular precursors were used to build up the ceria walls, and many synthetic routes to ceria nanocrystals are currently available in the literature.[45,46]

Two factors influence the increase in intercalation. In the first place, short diffusion path lengths induced by nanometer-scale domains should facilitate the kinetics of Li^+ insertion. Perhaps more importantly, however, is the fact that the entire nanoscale pore system can flex to accommodate the volume expansion associated with Li^+ insertion. In this way, creating materials with periodicity on two different length scales—both atomic and nanoscale—provides a new route to alleviate the strain associated with cation insertion in electrochemical materials, especially those without preferred crystallographic directions for ion transport. It is our hope that these concepts and approaches can help lead to finding or "re-discovering" metal oxide materials for battery and supercapacitor applications.

EXPERIMENTAL SECTION

Materials. $CeCl_3 \cdot 7H_2O$ was purchased from Sigma-Aldrich. $H(CH_2CH_2CH_2(CH)CH_2CH_3)_{89}(OCH_2CH_2)_{79}OH$ (also referred to as KLE) was used as organic template.[47]

Thin Film Synthesis. In a typical synthesis, 100 mg of KLE dissolved in 4 mL of EtOH is combined with 600 mg of $CeCl_3 \cdot 7H_2O$. Once the solution is homogeneous, 200 mg of double distilled H_2O is added. Thin films are produced *via* dip-coating on polar substrates in a controlled environment. The substrates included fused silica, fluorine-doped SnO_2 glass, (100)-oriented silicon wafer, and platinized silicon wafer. Optimal conditions occur with 15% relative humidity and a constant withdrawal rate of 1−10 mm/s. For best results, films are calcined using a 1 h ramp to 600 °C followed by a 10 min soak. Nontemplated CeO_2 films are produced without any KLE but under otherwise identical conditions.

Methods. TEM and field emission SEM images were taken with a Zeiss EM 912Ω microscope at an acceleration voltage of 120 kV and a LEO440 instrument equipped with an InLens detector (acceleration voltage = 2.0 kV), respectively. Tapping-mode

AFM images were acquired with a multimode AFM from Vecco Instruments employing Olympus microcantilevers (resonance frequency = 300 kHz, force constant = 42 N/m). *In situ* WAXS measurements were carried out at the Elettra Synchrotron Light Source. 2D-SAXS patterns were collected on Beamline 1-4 at the Stanford Synchrotron Radiation Laboratory. 1D-SAXS measurements were performed on an XPert PRO MPD diffractometer from Panalytical instruments utilizing a mirror−mirror ($\theta-2\theta$) geometry for the high resolution. The film thickness was determined using a Vecco Dektak 6 M profilometer.

Electrochemical experiments were carried out in an argon-filled glovebox in a three-electrode cell using a PAR EG&G 273 potentiostat. The working electrode area was set at 1 cm^2, and a lithium foil several times the area of the working electrode was used as the counter electrode; the reference electrode was a lithium wire. The electrolyte solution was 1.0 M $LiClO_4$ in propylene carbonate (PC). Cyclic voltammetry was used to study the electrochemical behavior using cutoff voltages at 4.0 and 1.3 V *vs* Li/Li^+. Electrochemical impedance spectroscopy measurements (Solartron 1252) were performed in a frequency range from 100 kHz to 0.1 Hz with a dc bias ranging from 1.5 to 4.0 V *vs* Li/Li^+. Experimental data were numerically modeled using ZView.

Acknowledgment. The authors thank T. E. Quickel, N. Pinna and H. Amenitsch for their assistance in materials preparation and measurements. This work was supported by the Office of Naval Research (S.T. and B.D., synthesis and measurements), by the Center for Molecularly Assembled Material Architectures for Solar Energy Production, Storage and Carbon Capture, an Energy Frontier Research Center funded by the U.S. Department of Energy, Office of Science, Office of Basic Energy Sciences under award DE-SC0001342 (S.T. and B.D., measurements and analysis), and by the Fonds der Chemischen Industrie through a Liebig fellowship (T.B.). Portions of this research were carried out at the Stanford Synchrotron Radiation Laboratory, a national user facility operated by Stanford University on behalf of the U.S. Department of Energy, Office of Basic Energy Sciences.

REFERENCES AND NOTES

1. Brinker, C. J.; Lu, Y. F.; Sellinger, A.; Fan, H. Y. Evaporation-Induced Self-Assembly: Nanostructures Made Easy. *Adv. Mater.* **1999**, *11*, 579–585.
2. Ogawa, M. Preparation of Layered Silica-Dialkyldimethylammonium Bromide Nanocomposites. *Langmuir* **1997**, *13*, 1853–1855.
3. Richman, E. K.; Brezesinski, T.; Tolbert, S. H. Vertically Oriented Hexagonal Mesoporous Films Formed through Nanometre-Scale Epitaxy. *Nat. Mater.* **2008**, *7*, 712–717.
4. Crepaldi, E. L.; Soler-Illia, G. J. A. A.; Grosso, D.; Sanchez, C. Nanocrystallised Titania and Zirconia Mesoporous Thin Films Exhibiting Enhanced Thermal Stability. *New J. Chem.* **2003**, *27*, 9–13.
5. Li, D. L.; Zhou, H. S.; Honma, I. Design and Synthesis of Self-Ordered Mesoporous Nanocomposite through Controlled *In-Situ* Crystallization. *Nat. Mater.* **2004**, *3*, 65–72.
6. Sallard, S.; Brezesinski, T.; Smarsly, B. M. Electrochromic Stability of WO_3 Thin Films with Nanometer-Scale Periodicity and Varying Degrees of Crystallinity. *J. Phys. Chem. C* **2007**, *111*, 7200–7206.
7. Brezesinski, T.; Groenewolt, M.; Gibaud, A.; Pinna, N.; Antonietti, M.; Smarsly, B. Evaporation-Induced Self-Assembly (EISA) at Its Limit: Ultrathin, Crystalline Patterns by Templating of Micellar Monolayers. *Adv. Mater.* **2006**, *18*, 2260–2263.
8. Sanchez, C.; Boissiere, C.; Grosso, D.; Laberty, C.; Nicole, L. Design, Synthesis, and Properties of Inorganic and Hybrid Thin Films Having Periodically Organized Nanoporosity. *Chem. Mater.* **2008**, *20*, 682–737.
9. Brezesinski, T.; Antonietti, M.; Smarsly, B. M. Self-Assembled Metal Oxide Bilayer Films with Single-Crystalline Overlayer Mesopore Structure. *Adv. Mater.* **2007**, *19*, 1074–1078.
10. Nolan, M.; Parker, S. C.; Watson, G. W. Reduction of NO_2 on Ceria Surfaces. *J. Phys. Chem. B* **2006**, *110*, 2256–2262.
11. Jasinski, P.; Suzuki, T.; Anderson, H. U. Nanocrystalline Undoped Ceria Oxygen Sensor. *Sens. Actuators, B* **2003**, *95*, 73–77.
12. Leah, R. T.; Brandon, N. P.; Aguiar, P. Modelling of Cells, Stacks and Systems Based around Metal-Supported Planar IT-SOFC Cells with CGO Electrolytes Operating at 500−600 Degrees C. *J. Power Sources* **2005**, *145*, 336–352.
13. Berton, M. A. C.; Avellaneda, C. O.; Bulhoes, L. O. S. Thin Film of CeO_2-SiO_2: A New Ion Storage Layer for Smart Windows. *Sol. Energy Mater. Sol. Cells* **2003**, *80*, 443–449.
14. Keomany, D.; Petit, J. P.; Deroo, D. Electrochemical Insertion in Sol−Gel Made CeO_2−TiO_2 from Lithium Conducting Polymer Electrolyte—Relation with the Material Structure. *Sol. Energy Mater. Sol. Cells* **1995**, *36*, 397–408.
15. Tarascon, J. M.; Armand, M. Issues and Challenges Facing Rechargeable Lithium Batteries. *Nature* **2001**, *414*, 359–367.
16. Whittingham, M. S. Lithium Batteries and Cathode Materials. *Chem. Rev.* **2004**, *104*, 4271–4301.
17. Arico, A. S.; Bruce, P.; Scrosati, B.; Tarascon, J. M.; Van Schalkwijk, W. Nanostructured Materials for Advanced Energy Conversion and Storage Devices. *Nat. Mater.* **2005**, *4*, 366–377.
18. Jamnik, J.; Maier, J. Nanocrystallinity Effects in Lithium Battery Materials—Aspects of Nano-Ionics. Part IV. *Phys. Chem. Chem. Phys.* **2003**, *5*, 5215–5220.
19. Brezesinski, T.; Wang, J.; Polleux, J.; Dunn, B.; Tolbert, S. H. Templated Nanocrystal-Based Porous TiO_2 Films for Next-Generation Electrochemical Capacitors. *J. Am. Chem. Soc.* **2009**, *131*, 1802–1809.
20. Conway, B. E.; Birss, V.; Wojtowicz, J. The Role and Utilization of Pseudocapacitance for Energy Storage by Supercapacitors. *J. Power Sources* **1997**, *66*, 1–14.
21. Wang, J.; Polleux, J.; Lim, J.; Dunn, B. Pseudocapacitive Contributions to Electrochemical Energy Storage in TiO_2 (Anatase) Nanoparticles. *J. Phys. Chem. C* **2007**, *111*, 14925–14931.
22. Brezesinski, T.; Smarsly, B.; Groenewolt, M.; Antonietti, M.; Grosso, D.; Boissière, C.; Sanchez, C. The Generation of Mesoporous CeO_2 with Crystalline Pore Walls Using Novel Block Copolymer Templates. *Stud. Surf. Sci. Catal.* **2005**, *156*, 243–248.
23. Miyata, H.; Suzuki, T.; Fukuoka, A.; Sawada, T.; Watanabe, M.; Noma, T.; Takada, K.; Mukaide, T.; Kuroda, K. Silica Films with Single-Crystalline Mesoporous Structure. *Nat. Mater.* **2004**, *3*, 651–656.
24. Lyons, D. M.; Ryan, K. M.; Morris, M. A. Preparation of Ordered Mesoporous Ceria with Enhanced Thermal Stability. *J. Mater. Chem.* **2002**, *12*, 1207–1212.
25. Porqueras, I.; Person, C.; Corbella, C.; Vives, M.; Pinyol, A.; Bertan, E. Characteristics of E-Beam Deposited Electrochromic CeO_2 Thin Films. *Solid State Ionics* **2003**, *165*, 131–137.
26. Orel, Z. C.; Orel, B. Structural and Electrochemical Properties of CeO_2 and Mixed CeO_2/SnO_2 Coatings. *Sol. Energy Mater. Sol. Cells* **1996**, *40*, 205–219.
27. Bard, A. J.; Faulkner, L. R. *Electrochemical Methods: Fundamentals and Applications*; John Wiley & Sons: New York, 1980.
28. Lindstrom, H.; Sodergren, S.; Solbrand, A.; Rensmo, H.; Hjelm, J.; Hagfeldt, A.; Lindquist, S. E. Li^+ Ion Insertion in TiO_2 (Anatase). 2. Voltammetry on Nanoporous Films. *J. Phys. Chem. B* **1997**, *101*, 7717–7722.
29. Liu, T. C.; Pell, W. G.; Conway, B. E.; Roberson, S. L. Behavior of Molybdenum Nitrides as Materials for Electrochemical Capacitors—Comparison with Ruthenium Oxide. *J. Electrochem. Soc.* **1998**, *145*, 1882–1888.
30. Gibot, P.; Casas-Cabanas, M.; Laffont, L.; Levasseur, S.; Carlach, P.; Hamelet, S.; Tarascon, J. M.; Masquelier, C. Room-Temperature Single-Phase Li Insertion/Extraction in Nanoscale Li_xFePO_4. *Nat. Mater.* **2008**, *7*, 741–747.

31. Brett, C. M. A.; Brett, A. M. O. *Electrochemistry: Principles, Methods, and Applications*; Oxford University Press: New York, 1993.
32. Miller, J. M.; Dunn, B. Morphology and Electrochemistry of Ruthenium/Carbon Aerogel Nanostructures. *Langmuir* **1999**, *15*, 799–806.
33. Conway, B. E. *Electrochemical Supercapacitors: Scientific Fundamentals and Technological Applications*; Kluwar Academic/Plenum Publishers: New York, 1999.
34. Kirsch, B. L.; Chen, X.; Richman, E. K.; Gupta, V.; Tolbert, S. H. Probing the Effects of Nanoscale Architecture on the Mechanical Properties of Hexagonal Silica/Polymer Composite Thin Films. *Adv. Funct. Mater.* **2005**, *15*, 1319–1327.
35. Fan, H. Y.; Hartshorn, C.; Buchheit, T.; Tallant, D.; Assink, R.; Simpson, R.; Kisse, D. J.; Lacks, D. J.; Torquato, S.; Brinker, C. J. Modulus-Density Scaling Behaviour and Framework Architecture of Nanoporous Self-Assembled Silicas. *Nat. Mater.* **2007**, *6*, 418–423.
36. Senter, R.; Tolbert, S. H. Manuscript in preparation.
37. Timoshenko, S. In *Strength of Materials*, 3rd ed.; Van, D., Ed.; Nostrand Reinhold: New York, 1956.
38. http://hyperphysics.phy-astr.gsu.edu/hbase/tables.
39. Roberts, R. B. Thermal Expansion Reference Data: Silicon 300−850K. *J. Phys. D: Appl. Phys.* **1981**, *14*, L163–L166.
40. Chavan, S. V.; Mathews, M. D.; Tyagi, A. K. Phase Relations and Thermal Expansion Studies in the Ceria−Yttria System. *J. Am. Ceram. Soc.* **2004**, *87*, 1977–1980.
41. Gross, J.; Fricke, J. Thermal-Expansion of Carbon and Silica Aerogels above Room-Temperature. *J. Non-Cryst. Solids* **1995**, *186*, 301–308.
42. Sato, K.; Yugami, H.; Hashida, T. Effect of Rare-Earth Oxides on Fracture Properties of Ceria Ceramics. *J. Mater. Sci.* **2004**, *39*, 5765–5770.
43. Puchegger, S.; Brandhuber, D.; Husing, N.; Peterlik, H. Changing Poisson's Ratio of Mesoporous Silica Monoliths with High Temperature Treatment. *J. Non-Cryst. Solids* **2006**, *352*, 5251–5256.
44. Laberty-Robert, C.; Long, J. W.; Lucas, E. M.; Pettigrew, K; Thomas, A.; Stroud, R. M.; Doescher, M. S.; Rolison, D. R. Sol−Gel-Derived Ceria Nanoarchitectures: Synthesis, Characterization, and Electrical Properties. *Chem. Mater.* **2006**, *18*, 50–58.
45. Yu, T. Y.; Joo, J.; Park, Y. I.; Hyeon, T. Large-Scale Nonhydrolytic Sol−Gel Synthesis of Uniform-Sized Ceria Nanocrystals with Spherical, Wire, and Tadpole Shapes. *Angew. Chem., Int. Ed.* **2005**, *44*, 7411–7414.
46. Zhang, F.; Jin, Q.; Chan, S. W. Ceria Nanoparticles: Size, Size Distribution, and Shape. *J. Appl. Phys.* **2004**, *95*, 4319–4326.
47. Fattakhova-Rohlfing, D.; Brezesinski, T.; Rathousky, J.; Feldhoff, A.; Oekermann, T.; Wark, M.; Smarsly, B. Transparent Conducting Films of Indium Tin Oxide with 3D Mesopore Architecture. *Adv. Mater.* **2006**, *18*, 2980–2983.